

RESEARCH ARTICLE

Transitional Separated Flow Over Low-Aspect-Ratio NACA0012 Wings

BERKAN ANILIR¹, TAIBA KOUSER², DILEK FUNDA KURTULUS¹,
SRIKANTH GOLI², MUHAMMAD SABIH², IMIL HAMDA IMRAN³,
AZHAR M. MEMON², AND LUAI M. ALHEMS²

¹Aerospace Engineering Department, METU, 06800 Ankara, Türkiye

²Applied Research Center for Metrology, Standards and Testing, King Fahd University of Petroleum and Minerals (KFUPM), Dhahran 31261, Saudi Arabia

³Department of Electrical Engineering, College of Engineering, King Faisal University, Al Ahsa 31982, Saudi Arabia

Corresponding author: Taiba Kouser (taiba.kouser@kfupm.edu.sa)

This work was supported in part by the Research, Development, and Innovation Authority (RDIA), Saudi Arabia, under Project 12922-KFUPM-2023-KFUPM-R-3-1-EI; and in part by The Applied Research Center for Metrology, Standards and Testing (ARCMST), King Fahd University of Petroleum and Minerals (KFUPM). The work of Imil Hamda Imran was supported by the Deanship of Scientific Research, Vice Presidency for Graduate Studies and Scientific Research, King Faisal University, Saudi Arabia, under Grant KFU260349.

ABSTRACT Three-dimensional transitional separated flow over low-aspect-ratio NACA0012 wings (semi-aspect ratios of $sAR = 1$ and 2) is numerically investigated at Reynolds numbers of 1×10^4 and 4×10^4 , across a range of angles of attack from 10° to 20° . The numerical simulations are performed by solving the unsteady Reynolds-averaged Navier-Stokes (URANS) equations, employing the transitional turbulence model of shear stress transport (SST) $\gamma - Re_\theta$ to simulate the turbulent flow and predict the laminar-to-turbulent transition. It is observed that the lower aspect ratio wing ($sAR = 1$) produces lower lift and drag coefficients than the higher aspect ratio wing ($sAR = 2$), regardless of the Reynolds number. For $sAR = 1$, the lift coefficient increases monotonically with angle of attack, whereas $sAR = 2$ exhibits the opposite trend at $Re = 1 \times 10^4$. At lower aspect ratios, the downwash induced by the wingtip vortices affects a broader spanwise region. The spike in the sectional lift coefficient is found closer to the root for $sAR = 1$. Moreover, the separation and transition points are observed earlier for the higher aspect ratio wing. For $sAR = 1$, the wake remains steady under all tested conditions due to the strong downwash effect. This steady wake behavior may be influenced by the turbulence modeling, which can suppress low-frequency vortex shedding compared to LES or DNS simulations. In contrast, the unsteady flow and Karman vortex shedding appear across the midspan when the downwash weakens for $sAR = 2$.

INDEX TERMS Low aspect ratio wing, laminar-to-turbulent transition, separated flow, NACA0012.

I. INTRODUCTION

The low-speed flow over aerodynamic surfaces has achieved tremendous interest with a significant rise in research and development efforts focused on micro aerial vehicles (MAVs). These vehicles naturally function at low Reynolds numbers, where conventional aerodynamic theories may not be fully applicable; thus, the laminar-to-turbulent transition, flow separation, and vortex dynamics must be accurately analyzed for optimizing their performance, stability, and energy efficiency. Therefore, it is essential to understand low-

speed aerodynamics in order to advance the MAV design and improve their operational capabilities [1].

The MAV platforms are often employed in low aspect ratio (AR) wings, especially for fixed-wing designs such as Black Widow [2], TH360 [3], NPS [4], Bee [5], and MicroBrosh [6]. The low AR wings experience stronger tip vortices compared to high-aspect ratio wings, which causes highly three-dimensional flow. In the literature, there are comparatively fewer studies for low Re flow past a low-aspect ratio finite wing. One of the earliest studies on this topic is the wind tunnel experiments of Torres and Mueller [7]. The aerodynamic coefficients of various wing platforms with a wide range of aspect ratios ranging from 0.5 to 2 have

The associate editor coordinating the review of this manuscript and approving it for publication was Guillermo Valencia-Palomo¹.

been investigated at Reynolds numbers between $Re = 7 \times 10^4$ and 2×10^5 . The nonlinear lift curves and greater values of the stall angle of attack (α_{stall} , around 15° to 25° increment), therewith the maximum lift (C_{Lmax} , around a value of 0.35 increment) are observed for the rectangular wings of aspect ratio below 1.25. Wind tunnel experiments of Mizoguchi and Itoh [8] at lower Reynolds number range between $Re = 2.6 \times 10^4$ and 7.6×10^4 also agree well in the discussion of the influence of low-aspect ratio on α_{stall} and C_{Lmax} . The reason is attributed to flow separation suppression by strong wing-tip vortices, without a qualitative explanation of the flowfield. Also, they observed no significant difference in the aerodynamic characteristics for the wings with $AR \geq 3$. Similar experiments but with higher aspect ratio wings, where $AR = 2 - 5$, were also performed by Ananda et al. [9], and no significant variation in C_{Lmax} was observed. Okamoto and Azuma [10] experimentally investigated various wing platforms (elliptical, rectangular, swept, and triangular wings) with a wide range of aspect ratios ($AR = 0.5 - 8$) at Reynolds numbers in the order of $1 - 2 \times 10^4$. They found that the decrease in Reynolds number leads to a marginal decline in C_{Lmax} for a low AR wing. Okamoto et al. [11] performed wind tunnel experiment at Reynolds numbers lower than those of [7], [8], and [9] between $Re = 1 \times 10^3$ and 1×10^4 on $AR = 0.5 - 2$. Their findings resemble those of Torres and Mueller [7] in terms of stall characteristics, even though they studied much lower Reynolds numbers. Besides, the detrimental influence of Reynolds number drop on C_{Lmax} ascribed to the disappearance of vortex lift is observed.

The following publications provide detailed explanations of the flow physics behind the interaction between a separated flow and a tip vortex over low AR wings through computational or experimental investigations. Among the first ones is Direct Numerical Simulations (DNS) of Taira and Colonius [12] for a full-span rectangular flat plate wing with AR between 1 and 4 for $Re = 3 \times 10^2$ and 5×10^2 at post-stall regimes. They found that the tip vortices can lead to flow stabilization and leading-edge separation suppression at $AR = 1$, whereas the vortices are shed but not similar to two-dimensional Karman vortex street at $AR = 4$. Zhang et al. [13] have also demonstrated the influence of aspect ratio and angle of attack on the wake structure and the flow separation at $Re = 4 \times 10^2$. The wing was a half-wing and constructed with an NACA0015 airfoil. They demonstrated that the wake structures are strongly dependent on aspect ratio and angle of attack. The wake can maintain its steady-state status at moderate angles of attack for LAR due to a strong downwash from the tip vortex, preventing the leading and trailing-edge vortex shedding from acquiring the whole span. Smith and Taira [14] investigated the flow over a finite NACA0012 with $sAR = 2$ using high-fidelity simulations at a broader and higher Reynolds number interval ($6 \times 10^2 \leq Re \leq 1 \times 10^4$) than those of [12] and [13] at $\alpha = 14^\circ$. The results show that the increase in Reynolds number leads to a stronger wing

tip vortex, therewith wake compression near the tip, thus enhancing vortex lift. The wake vortex structures past half-finite rectangular NACA0012 wing ($0.25 \leq sAR \leq 7.5$) are identified for $Re = 1 \times 10^3$ at $0^\circ \leq \alpha \leq 14^\circ$ by Pandi and Mittal [15]. The flow is fully steady for $sAR = 0.25$ and 0.5 regardless of α , whereas the wake consists of one cell without dislocations for $sAR = 1$ and 2 when $\alpha \geq 10^\circ$. As sAR increases, the various types of vortex dislocations appear. The PIV measurements of Zhu et al. [16], [17] for low AR wings at around $Re = 6 \times 10^3$ reveal the detailed evolution routine of the vortical structures and interaction between spanwise fluid transport and downwash due to the tip vortex. Besides, there are also several studies in the literature that focus on triglobal stability analysis on the flow over finite wing [18], [19], [20], [21].

Another key feature of low Reynolds number flow is that the laminar separation bubble (LSB) commonly occurs at $Re \leq 5 \times 10^5$. Laminar separation bubble is characterized by a separated flow region enclosed between the laminar separation and turbulent reattachment locations, as well as the laminar-to-turbulent transition within the recirculating flow [22], [23], [24]. The presence of LSB often leads to a detrimental influence on the aerodynamic performance, decrease in lift-to-drag ratio; therefore, it attracts great attention in both experimental [25], [26], [27], [28], [29], [30], [31], [32], [33] and numerical [34], [35], [36], [37], [38], [39], [40] studies. The development of LSB on the half wing with $sAR = 2.5$ at $Re = 1.25 \times 10^5$ and $\alpha = 6^\circ$ are distinguishably investigated via PIV and surface pressure measurements near the root, mid and tip sections separately in the three papers of Toppings and Yarusevych [29], [30], [31]. They compared the finite wing with the two-dimensional airfoil at the same local effective angle of attack. The measurement shows a similarity in the location of LSB, whereas displacement thickness and reverse flow magnitude show significant differences. Outside the wall junction and wing-tip vortex affected region, where the spanwise velocity gradients are limited, the spanwise variation of the vortex shedding characteristics remains mostly constant. On the other hand, the wing tip vortex leads to a decrease in separation bubble thickness and transition delay, which are more significant in the region of $0.5c$ ($0.2b$) from the tip and exhibit critical LSB structure modification (complete separation suppression) within $0.2c$ ($0.08b$) from the tip.

The aforementioned literature shows that the studies on the low-aspect-ratio wing focused either on very low Reynolds number regimes ($Re < 10^4$) using high-fidelity simulations or on moderate Reynolds numbers ($Re > 10^5$) using PIV measurements or aerodynamic coefficients. Therefore, the three-dimensional transitional separated flowfield over low-aspect ratio wings at Reynolds numbers between very low to moderate regimes remains largely unexplored.

The objective of the current study is to numerically explore the aerodynamics of a low-aspect-ratio finite NACA0012 wing under transitional separated flow. To achieve the

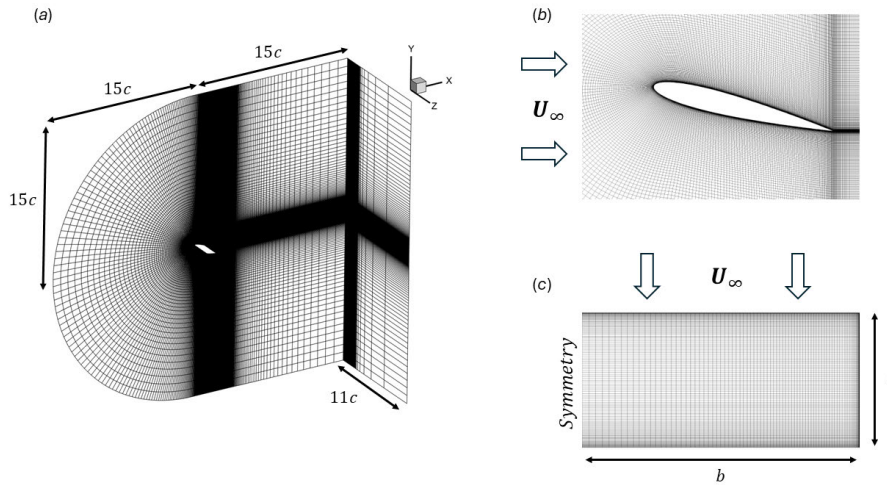


FIGURE 1. (a) Computational domain (b) side view of domain at $z/c = 0.5$ and (c) wing's surface grid.

objective, the transitional URANS simulations are conducted by using ANSYS Fluent v23.2 and turbulence model of shear stress transport (SST) $\gamma - Re_\theta$ on the finite wing with $sAR = 1$ and $sAR = 2$, and two-dimensional airfoil at $Re = 1 \times 10^4 - 4 \times 10^4$ and $\alpha = 10^\circ - 20^\circ$.

II. METHODOLOGY

The transitional incompressible flow over a finite rectangular wing of half-span b and chord length $c = 0.1\text{ m}$, with a NACA0012 airfoil is studied at two values of chord and freestream velocity (U_∞) based Reynolds number, $Re = \rho U_\infty c / \mu = 1 \times 10^4$ and 4×10^4 . The airfoil is a logical choice for basic fluid dynamics research due to its analytical form and widespread usage in the literature. The half-wing model is simulated to reduce computational cost; thus, a symmetry flow boundary condition is imposed at the root of the wing. The high-order simulations of Pandi and Mittal [15], [41] demonstrate the validity of symmetry boundary conditions at the root, and they found no difference between the half-wing and full-wing simulations. The semi-aspect ratios of the wings are set to $sAR = b/c = 1$ and 2 . All wings considered herein present wing geometries with a sharp trailing edge and a straight-cut wing tip. They are rotated around the quarter chord point to provide the angle of attack, which is defined between the airfoil chord line and the freestream direction and set to $\alpha = 10^\circ, 15^\circ$ and 20° .

A. NUMERICAL SETUP

The numerical simulations are performed using a commercial finite volume solver of ANSYS Fluent v23.2 solving the unsteady Reynolds-averaged Navier-Stokes (URANS) equations and using the shear stress transport (SST) $\gamma - Re_\theta$ turbulence model. The numerical solution is obtained by evaluating the gradients using the Least Squares Cells-Based scheme. The second-order upwind scheme was adopted as

the method to discretize pressure, momentum, turbulent kinetic energy, specific dissipation rate, intermittency and momentum thickness Re equations. The transient formulation uses the second-order implicit iterative time advancement scheme (ITA). The advantage of the implicit scheme is that it is unconditionally stable with respect to time-step size [42]. To advance the simulation in time, the time step size of $\Delta t = 0.001\text{ s}$ is chosen, which corresponds to a Courant-Friedrichs-Lewy (CFL) number less than 10 everywhere in the domain ($CFL = u\Delta t / \Delta x \leq 10$) [43]. Pressure velocity coupling is done by the Coupled algorithm, and the details of the algorithm can be found in Ferziger et al. [44].

The governing equations for unsteady and incompressible flow are provided below. The continuity and Navier-Stokes equations in Cartesian coordinates are presented in Eqs. 1 and 2, respectively.

$$\frac{\partial U_j}{\partial x_j} = 0 \tag{1}$$

$$\frac{\partial U_i}{\partial t} + \frac{\partial}{\partial x_j} (U_j U_i) = -\frac{1}{\rho} \frac{\partial p}{\partial x_i} + \frac{\partial}{\partial x_j} \left[\nu_{\text{eff}} \left(\frac{\partial U_i}{\partial x_j} + \frac{\partial U_j}{\partial x_i} \right) \right] \tag{2}$$

where U is the local velocity, p is the pressure and $\nu_{\text{eff}} = \nu + \nu_t$ denotes the effective kinematic viscosity where ν is the molecular kinematic viscosity and ν_t is the turbulent eddy viscosity. The transport equations for $k - \omega$ SST model of Menter [45] one for turbulent kinetic energy (k) and one for specific dissipation rate (ω) are shown in Eqs. 3 and 4, respectively. The turbulent eddy viscosity is computed from Eq. 5.

$$\frac{\partial k}{\partial t} + \frac{\partial}{\partial x_j} (U_j k) = \tilde{P}_k - \beta^* k \omega + \frac{\partial}{\partial x_j} \left[(\nu + \sigma_k \nu_t) \frac{\partial k}{\partial x_j} \right] \tag{3}$$

$$\frac{\partial \omega}{\partial t} + \frac{\partial}{\partial x_j} (U_j \omega) = \frac{\gamma \omega \tilde{P}_k}{\nu_t} - \beta \omega^2 + \frac{\partial}{\partial x_j} \left[\left(\nu + \sigma_\omega \nu_t \right) \frac{\partial \omega}{\partial x_j} \right] + 2(1 - F_1) \frac{\sigma_{\omega 2}}{\omega} \frac{\partial k}{\partial x_j} \frac{\partial \omega}{\partial x_j} \quad (4)$$

$$\nu_t = \frac{a_1 k}{\max(a_1 \omega, \Omega F_2)} \quad (5)$$

where $\tilde{P}_k = 2\nu_t S_{ij} S_{ij}$ is the turbulent kinetic energy production rate, S_{ij} is the strain-rate tensor and Ω_{ij} is the rotation-rate tensor. F_1 and F_2 are the blending functions, and F_1 controls the utilisation of $k - \epsilon$ or $k - \omega$ models. F_1 is equal to 1 inside the boundary layer; therefore, the $k - \omega$ model is used. But, it gradually switches to 0 in the wake region where the $k - \epsilon$ model is used [45]. The $\gamma - Re_\theta$ SST transition turbulence model, which couples the $k - \omega$ SST model of Menter [45] with two transport equations, one for intermittency and one for transition momentum thickness Reynolds number ($\hat{Re}_{\theta t}$) [46].

$$\frac{\partial \gamma}{\partial t} + \frac{\partial}{\partial x_j} (U_j \gamma) = \tilde{P}_\gamma - \tilde{E}_\gamma + \frac{\partial}{\partial x_j} \left[\left(\nu + \frac{\nu_t}{\sigma_f} \right) \frac{\partial \gamma}{\partial x_j} \right] \quad (6)$$

$$\frac{\partial \hat{Re}_{\theta t}}{\partial t} + \frac{\partial}{\partial x_j} (U_j \hat{Re}_{\theta t}) = \tilde{P}_{\theta t} + \frac{\partial}{\partial x_j} \left[\left(\nu + \frac{\nu_t}{\sigma_{\theta t}} \right) \frac{\partial \hat{Re}_{\theta t}}{\partial x_j} \right] \quad (7)$$

where \tilde{P}_γ is the transition source term and \tilde{E}_γ is the destruction/relaminarization source term of the intermittency equation. $\tilde{P}_{\theta t}$ is the source term in the transition momentum thickness Reynolds number equation. The intermittency equation governs the onset of transition (when $\gamma > 0$), while the Re_θ equation determines where the transition begins to develop based on local flow characteristics and the level of freestream turbulence. This model is capable of representing both natural and bypass transition mechanisms in complex flow scenarios. However, it does not resolve the detailed physics of the laminar-to-turbulent transition. Instead, it relies on empirical correlations and experimental observations to approximate transition behavior within the RANS framework [46], [47].

B. GRID REFINEMENT AND VALIDATION STUDY

The grid refinement study has been performed on $sAR = 1$ wing at $Re = 1 \times 10^4$ and $\alpha = 20^\circ$. There are three different grids, namely the coarse grid, medium grid and fine grid, and their grid sizes are $300 \times 280 \times 70$, $360 \times 340 \times 95$ and $410 \times 390 \times 130$, respectively. The variation of the aerodynamic coefficients for those grid levels is shown in Table 1. It can be seen that the difference between the medium and fine grids is less than 1%; hence, the further part of the study was performed with the medium grid.

Figure 1 provides various views of computational domain and wing geometry. Initially, a fully structured two-dimensional grid is composed over the NACA0012 airfoil. This grid is then extruded in the spanwise direction to create the finite wing geometry and a three-dimensional domain.

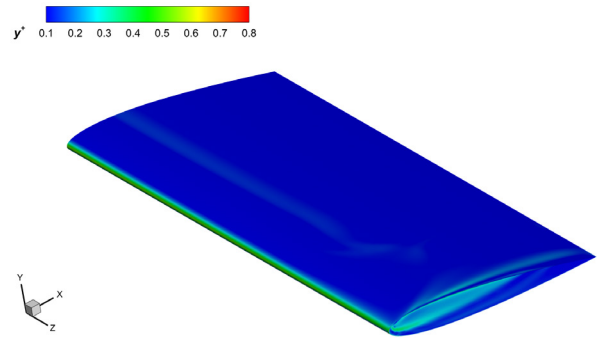


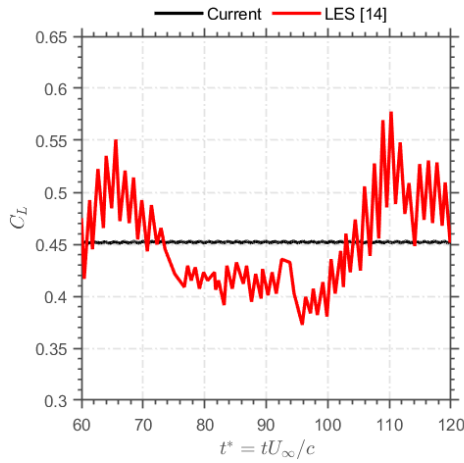
FIGURE 2. y^+ contours on $sAR = 2$ wing at $Re = 4 \times 10^4$ and $\alpha = 10^\circ$.

TABLE 1. Grid refinement study on $sAR = 1$ wing at $Re = 1 \times 10^4$ and $\alpha = 20^\circ$.

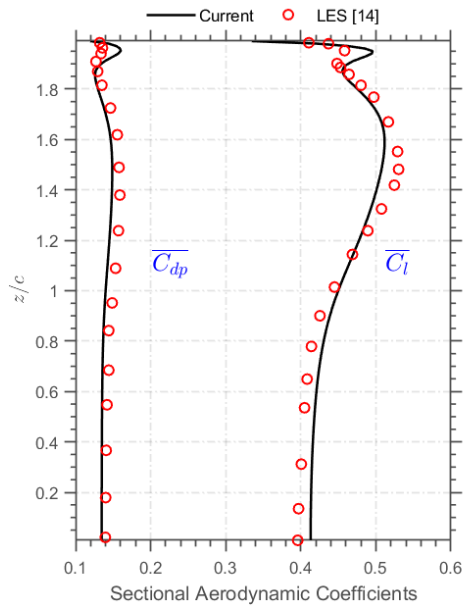
Grid Level	N_x	N_y	N_z	$\overline{C_L}$	$\overline{C_D}$
Coarse	300	280	70	0.519	0.243
Medium	360	340	95	0.488	0.233
Fine	410	390	130	0.486	0.233

The computational domain covers the largest domain being $(x/c, y/c, z/c) \in [-15, 15] \times [-15, 15] \times [0, 11]$, where x, y , and z are the streamwise, spanwise and vertical coordinates, respectively. The origin is placed at the leading edge of the wing root. The first cell height is chosen as $\Delta s = 0.001c$ to ensure that y^+ values remain below 1 for all cases (see Figure 2). The inlet and farfield boundaries are prescribed with a velocity inlet boundary condition where $U = (U_\infty, 0, 0)$. The outlet boundary is defined as a pressure outlet to facilitate the smooth convection of wake structures out of the domain. The symmetry is imposed at the wing root boundary, and the no-slip boundary condition (wall) is applied to the wing surface.

The model has been applied and validated in the literature at low Reynolds number flows by Counsil and Boulama [35], Zore et al. [47], Anilir et al. [48], [49], and Guney et al. [50]. In the current study, the simulations are validated against the recent LES analysis of Smith and Taira [14] at $\alpha = 14^\circ$ and $Re = 1 \times 10^4$ for $sAR = 2$ considering time history of lift coefficient, mean sectional lift coefficient and pressure-drag coefficient (see Figure 3). Although there are strong fluctuations in the lift due to the eddy structures captured by LES, the current URANS simulations can greatly demonstrate the mean quantities and vortex shedding frequency ($\overline{C_L} = 0.452$ and $St = fc/U_\infty = 0.66$ for URANS, and $\overline{C_L} = 0.452$ and $St = 0.69$ for LES). The sectional lift coefficient on the wing platform is non-monotonic, and it is maximum near the wingtip at around $1.6c$ and $1.5c$ for current and LES results, respectively. The main difference between the solutions is that the sudden rise in sectional aerodynamic coefficients due to the tip



(a)



(b)

FIGURE 3. Comparison of the current simulation against LES computations of Smith and Taira [14] in terms of (a) time history of the lift coefficient and (b) the spanwise distribution of mean sectional lift and pressure-drag coefficients at $\alpha = 14^\circ$ and $Re = 1 \times 10^4$ for $sAR = 2$.

vortex is observed in the vicinity of the wingtip, and this can be attributed to the geometric distinction (square-tip and rounded-tip). Despite the differences in the geometry, the overall agreement is quite good.

III. RESULTS AND DISCUSSION

This section outlines the transitional numerical results of a semispan NACA0012 wing with the parameters ranging $sAR = 1 - 2$, $Re = 1 \times 10^4 - 4 \times 10^4$ and $\alpha = 10^\circ - 20^\circ$, summarized in Figure 4. The important aerodynamic characteristics related to the aerodynamic force coefficients, sectional lift and drag coefficient distributions, laminar separation bubble characteristics (separation, laminar-to-turbulent transition and reattachment locations) and three-dimensional wake dynamics are described and discussed in detail.

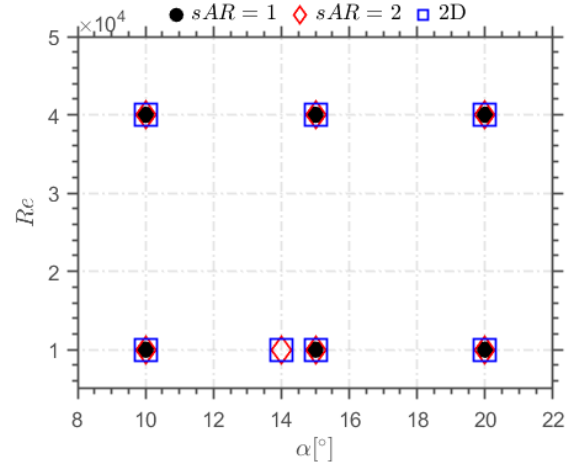


FIGURE 4. Map of Reynolds number and angle of attack analyzed.

A. MEAN AERODYNAMIC COEFFICIENTS

In this part of the paper, Figure 5 presents the variation of mean lift coefficient, mean drag coefficient and mean lift-to-drag ratio with respect to the angle of attack, as well as the influence of the aspect ratio and Reynolds number. It can be seen that the two-dimensional airfoil constantly produces higher lift and drag coefficients than the finite wing geometries at the same Reynolds number due to the reduction of the effective angle of attack along each spanwise location experienced by the finite wings. Similar findings are observed by Taira and Colonius [12], Zhang et al. [13], Zhang and Taira [51], and Pandi and Mittal [41] in their high order numerical simulations but at lower Reynolds numbers. The lift coefficient is also compared with the theoretical lift-curve slope prediction proposed in Eq. 8 by Helmbold [52] for unswept wings. These lines show the inviscid lift limit for the rectangular low AR wings.

$$C_{L\alpha} = 2\pi \frac{sAR}{\sqrt{1 + sAR^2} + 1} \quad (8)$$

It is noticed that the lower aspect ratio wing ($sAR = 1$) leads to smaller lift and drag coefficients than the higher aspect ratio wing ($sAR = 2$), regardless of Reynolds number. The lift coefficient monotonously increases with an increase in angle of attack at $Re = 1 \times 10^4$. However, for $Re = 4 \times 10^4$, the lift slightly increases for the wing $sAR = 1$, whereas it slightly decreases and then remains the same for the wing $sAR = 2$. The lift coefficient values are in the range of 0.40 to 0.48 and 0.50 to 0.54 for wings of $sAR = 1$ and $sAR = 2$, respectively. For $Re = 1 \times 10^4$, the lift coefficient ranges on a wider scale from 0.28 to 0.49 and 0.34 to 0.47 for $sAR = 1$ and $sAR = 2$, respectively. As the drag coefficient variation is examined in Figure 5b, the increase in Reynolds number and aspect ratio constantly leads to slightly higher drag coefficients similar to those findings of Taira and Colonius [12], Okamoto and Azuma [10], and Zhang et al. [13], [51] at high angles of attack. As shown in Figure 5c, the lift-to-drag ratio decreases with increasing angle of attack.

The wing with $sAR = 2$ has considerably higher lift-to-drag ratio at $\alpha = 10^\circ$, but this difference disappears as the angle of attack increases. Also, the maximum lift-to-drag ratio is probably achieved at $\alpha < 10^\circ$ for all conditions. The results of several related studies conducted under similar parameters are presented below to provide a comparative perspective. Ananda et al. [9] observed that the lift curve flattens around the value of 0.6 between $\alpha = 10^\circ$ and $\alpha = 20^\circ$ for a flat plate wing with $AR = 3$ at $Re = 8 \times 10^4$. This flattening was also observed by Mizoguchi and Itoh [8] for the same geometry but at lower Reynolds numbers of $Re = 2.6 \times 10^4$ and $Re = 5.2 \times 10^4$. Zhang et al. [13] noticed that the lift coefficient values between $\alpha = 10^\circ$ and $\alpha = 20^\circ$ vary from around 0.25 to 0.35 and 0.30 to 0.45 for the NACA0015 wing with $sAR = 1$ and $sAR = 2$, respectively; for a very low Reynolds number of $Re = 4 \times 10^2$.

The mean sectional lift ($\overline{C_l}$) and mean sectional drag coefficients ($\overline{C_d}$) are examined in Figure 6. These coefficients are calculated by nondimensionalizing the sectional mean lift ($\overline{L'}$) and mean drag forces ($\overline{D'}$) with respect to the product of dynamic pressure (q_∞) and chord length, as shown in Eqs. 9 and 10.

$$\overline{C_l} = \frac{\overline{L'}}{q_\infty c} \quad (9)$$

$$\overline{C_d} = \frac{\overline{D'}}{q_\infty c} \quad (10)$$

All conditions experience a noticeable local lift increase near the wingtip as a result of the wing tip vortex. The sectional peak lift values linearly increase and become more prominent with the angle of attack. As described in the sectional lift coefficient curves in Figure 6b for $Re = 4 \times 10^4$ and $\alpha = 10^\circ$, the rectangular wings feature root-loaded lift distribution characteristic, which is monotonically decreasing lift curve from root to tip, and the mean sectional lift coefficient at the root section is very close to those of a two-dimensional airfoil values around 0.45 and 0.6 for $sAR = 1$ and $sAR = 2$, respectively. On the other hand, the non-monotonicity is observed for all other conditions. The sectional lift coefficient gradually increases until the spike, then begins to decay. This spike is associated with the vortex lift as a result of the wake compression near this region, as is denoted by Smith and Taira [14]. Similar phenomenon is observed by Zhang et al. [13], Pandi and Mittal [15], [41], Ribeiro et al. [20], and Lee et al. [53]. As the two wings are compared, it can be clearly seen that the $sAR = 2$ wing exhibits this local lift peak closer to the wing tip than the $sAR = 1$ wing. For $sAR = 1$ wings, the spike location moves toward the root from approximately 75% to 60% of the half span as the angle of attack increases at $Re = 4 \times 10^4$. However, it stays near 60% of the half span for $\alpha = 15^\circ$ and $\alpha = 20^\circ$, and is not observed for $\alpha = 10^\circ$ when $Re = 1 \times 10^4$. However, the drag coefficient shows much less variation along the span compared to the lift coefficient.

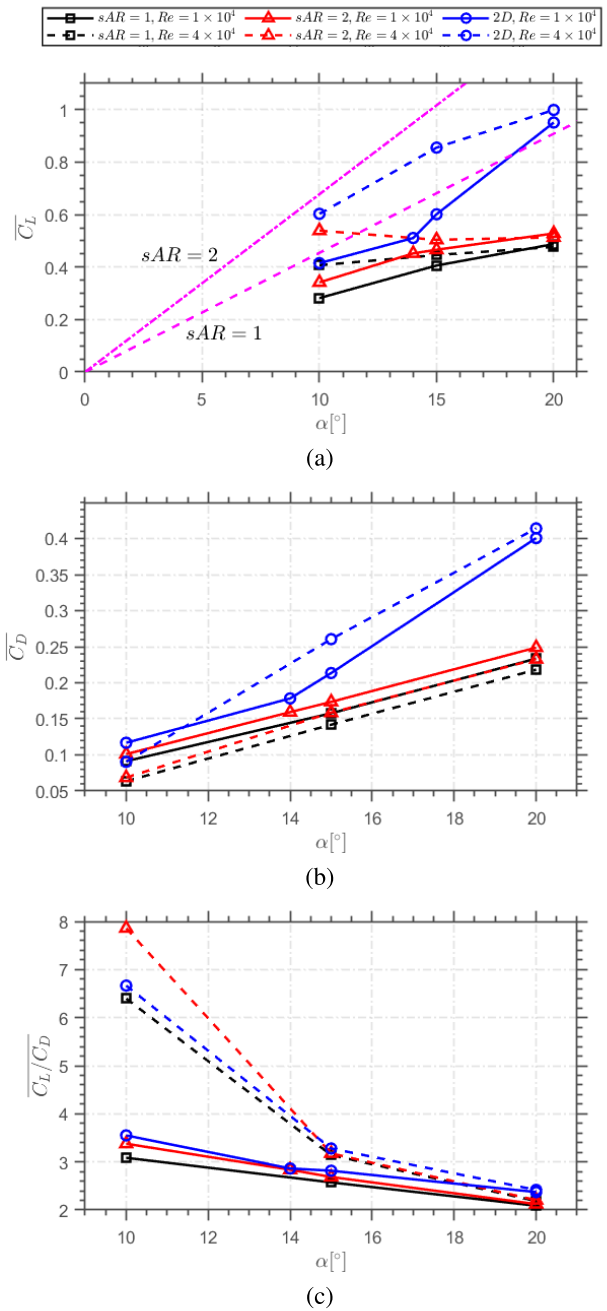


FIGURE 5. Variation of mean (a) lift coefficient, (b) drag coefficient and (c) lift-to-drag ratio with respect to angle of attack. The magenta colored --- and -.- lines in Figure a represent Helmbold’s [52] lift-curve slope predictions for $sAR = 1$ and $sAR = 2$ wings, respectively.

B. LAMINAR SEPARATION BUBBLE CHARACTERISTICS

The characterization of LSB is conducted based on the location of separation point, laminar-to-turbulent transition and reattachment point. The separation and reattachment points are determined by way of skin-friction coefficient distribution and confirmed by zero streamwise-velocity lines. Besides, there are several transition onset criteria used for laminar separation bubble based on the end of constant pressure [54], [55], location of maximum shape factor [27],

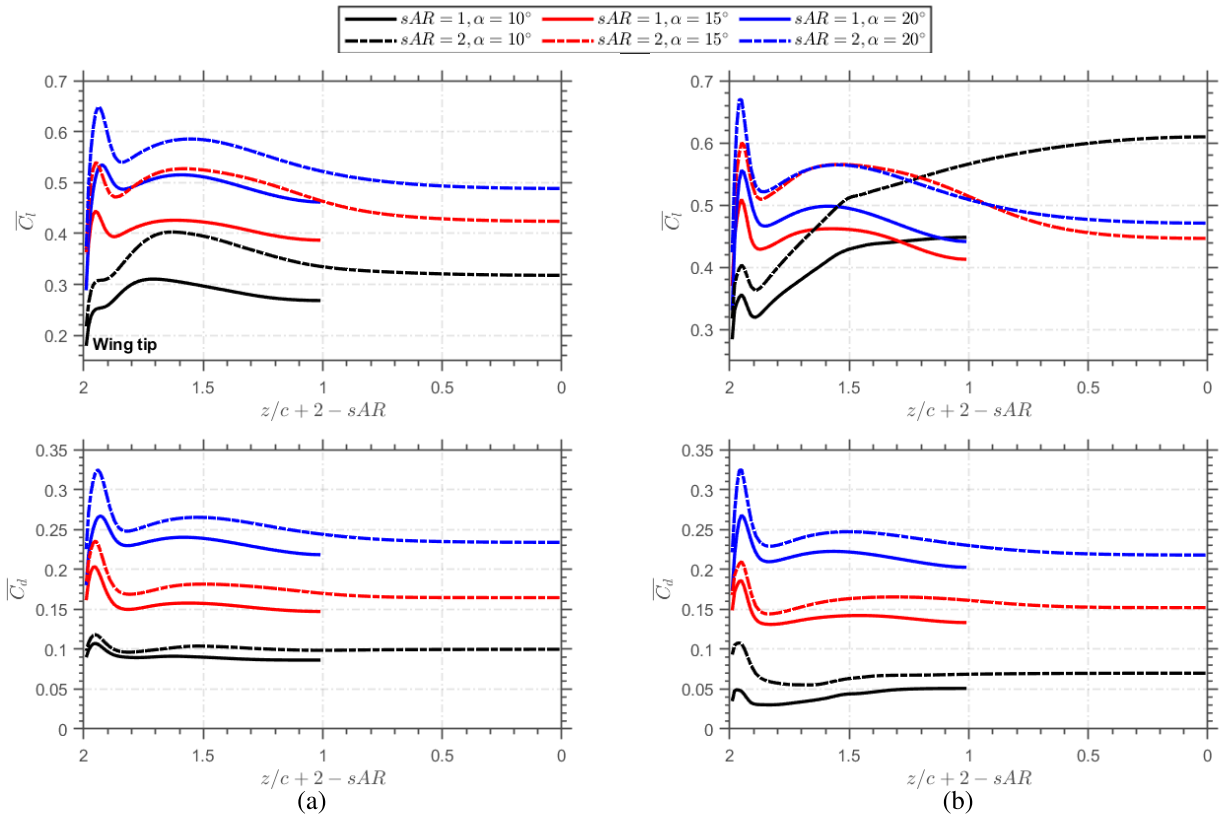


FIGURE 6. Variation of the mean sectional lift and drag coefficients along the spanwise direction for (a) $Re = 1 \times 10^4$, and (b) $Re = 4 \times 10^4$. The spanwise coordinates (z) are nondimensionalized using the wings' own half wingspan length, with $b = 1c$ for $sAR = 1$ and $b = 2c$ for $sAR = 2$. The wing root section is prescribed as $z/c = 0$.

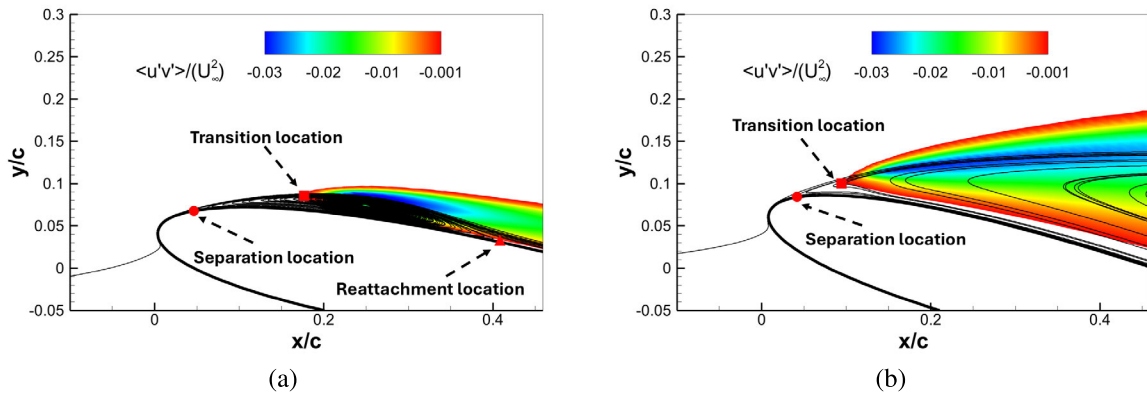


FIGURE 7. Transition point prediction based on normalized Reynolds stress criterion ($\overline{u'v'}/U_\infty^2 = -0.001$) under (a) short LSB and (b) fully separated flow.

[56], and location where $-\overline{u'v'}/U_\infty^2$ first attains 0.1% [33], [57], [58]. Due to expecting to observe both short leading edge LSB and fully separated flow (no reattachment), a Reynolds-stress threshold method, which is applicable for both these flow states, has been selected for the current study. Transition onset is estimated as the streamwise location where the normalized Reynolds stress ($\overline{u'v'}/U_\infty^2$) first reaches a value of -0.001 , as demonstrated in Figure 7.

Figure 8 shows the comparison of the spanwise variation of separation, transition and reattachment locations for $sAR = 1$ and $sAR = 2$ wings, and a two-dimensional airfoil at $Re = 4 \times 10^4$. For the lower Reynolds number condition of $Re = 1 \times 10^4$, since it is challenging to clearly identify the transition location under this condition due to the weak transitional features, this part only contains the results for the higher Reynolds number condition. If there is no LSB formation or

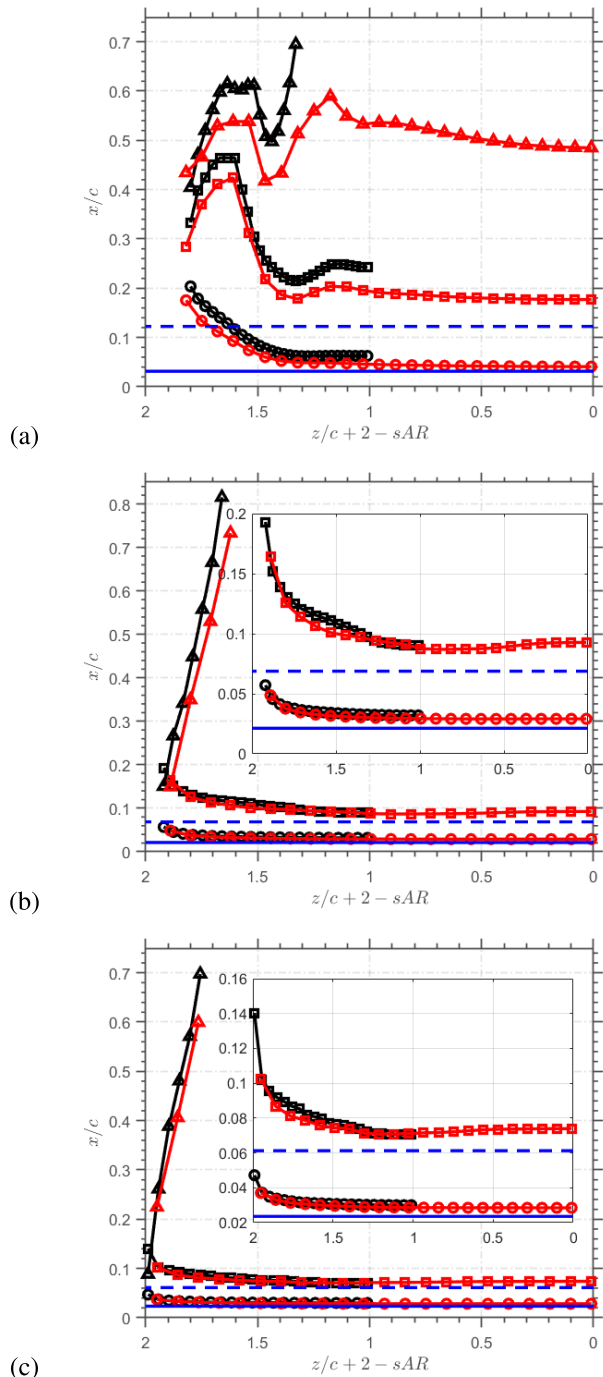


FIGURE 8. Locations of separation, transition, and reattachment points along the spanwise direction for (a) $\alpha = 10^\circ$, (b) $\alpha = 15^\circ$ and (c) $\alpha = 20^\circ$ at $Re = 4 \times 10^4$. The insets show the close view of the separation and transition points. Black line: $sAR = 1$, red line: $sAR = 2$, solid blue line: separation point for 2D airfoil, dashed blue line: transition point for 2D airfoil. \circ : separation point, \square : transition point, Δ : reattachment point. The wing root section (symmetry plane) and leading edge are prescribed at $z/c = 0$ and $x/c = 0$, respectively.

if an LSB occurs without reattachment, these regions are not marked with the symbol in the figures. At $\alpha = 10^\circ$, the finite

wings exhibit the typical LSB in the vicinity of the leading edge and the trailing edge bubble, whereas these two bubbles merge over the region from the root section to around $z/b = 0.35$ and consequently cover almost the whole suction side of the denoted wing region for $sAR = 1$. On the other hand, the transition in the separated laminar shear layer sufficiently energises the flow for $sAR = 2$; therefore, the reattachment occurs around the midspan. The two-dimensional airfoil also experiences similar coalescence, but the size of the separation is much more severe. Figure 9 shows the mean surface streamlines and pressure coefficient contours for those two wings at $\alpha = 10^\circ$. The surface streamlines depict the complex separation behavior, revealing a clear difference between the wings. A secondary separation region near the trailing edge is observed for $sAR = 2$, whereas no such secondary separation appears for $sAR = 1$. Moreover, the suction peak is slightly stronger for $sAR = 2$. Figure 10 presents the Reynolds stress cross-product $u'v'/U_\infty^2$ contours at large number of spanwise slices along with $U_x = 0$ isosurface colored by red.

It is also clear from Figure 8a that the variation in the separation point near the root is limited, and the separation for $sAR = 1$ and $sAR = 2$ begins approximately at $0.06c$ and $0.04c$, respectively. Moreover, the separation point is consistently located further downstream along each spanwise section of the finite wing, compared to the 2D airfoil, where separation initiates near $0.03c$. The tip vortex influences a larger portion and leads to delayed separation for $sAR = 1$ compared to a higher aspect ratio wing of $sAR = 2$. The separation point moves towards the trailing edge after $z/b = 0.35$ and is surpassed at $z/b = 0.8$ for $sAR = 1$; however, a similar movement of the separation is observed after $z/b = 0.7$, and the separation is retained until $z/b = 0.9$ for $sAR = 2$. Topping and Yarusevych [29] also stated that the downwash due to the tip vortex causes attached flow near the wing tip, but it also leads to noticeable spanwise changes in LSB parameters over the midspan region. As the transition locations are examined, it is observed that they occur further downstream for $sAR = 1$ than for $sAR = 2$, similar to those separation points. Both wings exhibit a gradual upstream shift of the transition point, reaching its furthest upstream location at the same position where the separation point delay is initially observed. Beyond this point, the transition locations shift rapidly toward the trailing edge. Beyond $z/b = 0.6$ for $sAR = 1$ and $z/b = 0.8$ for $sAR = 2$, the length of the LSB reduces; thus, the transition sharply moves towards the leading edge.

For $\alpha = 15^\circ$ and 20° , a large separation bubble without reattachment covers almost the whole suction side of the wings. Similar to the lower angle of attack of $\alpha = 10^\circ$, the separation and transition are delayed for LAR 3D wings compared to 2D airfoil under the same condition. The downwash from the tip vortex leads to flow reattachment near the tip, and the initial reattachment is observed closer to the wing root for $sAR = 1$ than for $sAR = 2$. As the

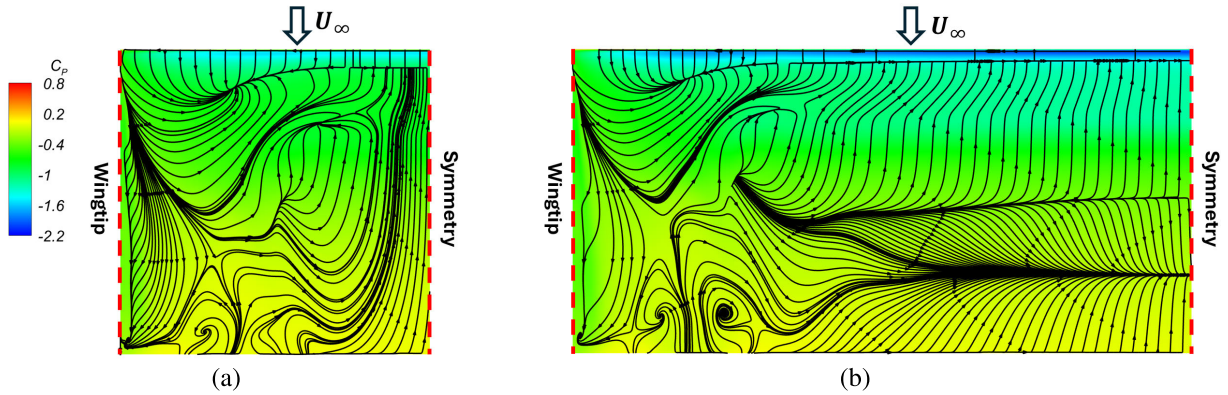


FIGURE 9. Mean skin-friction streamlines and surface pressure coefficient distributions on the suction side of (a) $sAR = 1$ and (b) $sAR = 2$ for $Re = 4 \times 10^4$ and $\alpha = 10^\circ$.

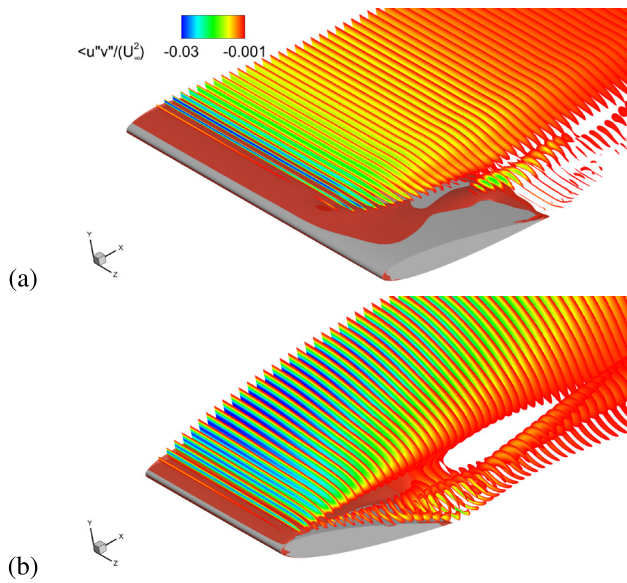


FIGURE 10. Reynolds stress contour and $U_x = 0$ isosurface over the wings of (a) $sAR = 2$ for $Re = 4 \times 10^4$ and $\alpha = 10^\circ$, and (b) $sAR = 1$ for $Re = 4 \times 10^4$ and $\alpha = 20^\circ$.

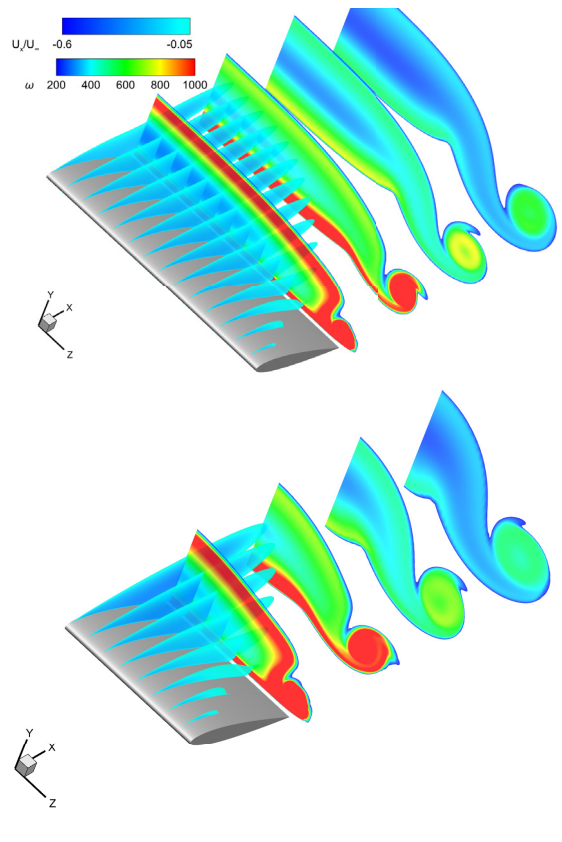


FIGURE 12. Separated flow region on the spanwise slice and specific dissipation rate (ω) on the wake contours for (a) $sAR = 2$ and (b) $sAR = 1$ at $Re = 4 \times 10^4$ and $\alpha = 20^\circ$.

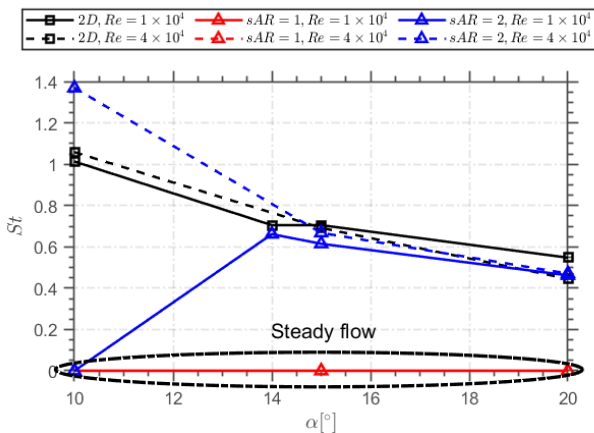


FIGURE 11. Variation of Strouhal number with respect to the angle of attack.

angle of attack increases, the completely attached flow region disappears.

C. WAKE VORTICAL STRUCTURES

In this section, the wake structures are examined and broadly classified into two types: steady and unsteady flows. According to the classification by Kurtulus [59], steady flow corresponds to a continuous vortex sheet (Mode I), while unsteady flow is associated with an alternating vortex shedding (Mode II). The steady flow regime is characterized by time-invariant aerodynamic coefficients and wake structure. In contrast, the unsteady flow exhibits periodic oscillations in the aerodynamic coefficients following an initial transient

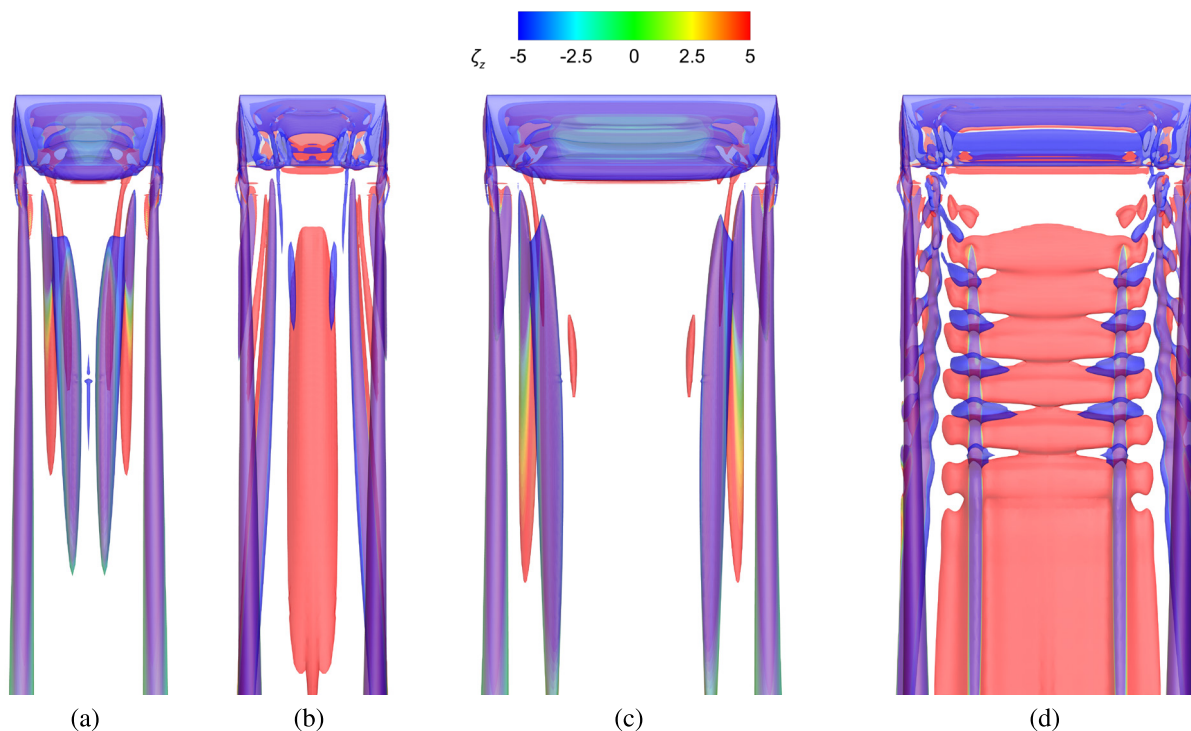


FIGURE 13. Top view of the vortical structure for (a) $sAR = 1, Re = 1 \times 10^4$, (b) $sAR = 1, Re = 4 \times 10^4$, (c) $sAR = 2, Re = 1 \times 10^4$, and (d) $sAR = 2, Re = 4 \times 10^4$ at $\alpha = 10^\circ$. The isosurface of $Q = 0.25$ is visualised and colored with $\zeta_z = \pm 5$. The full span wings are displayed for better visualization by applying a mirror on the root.

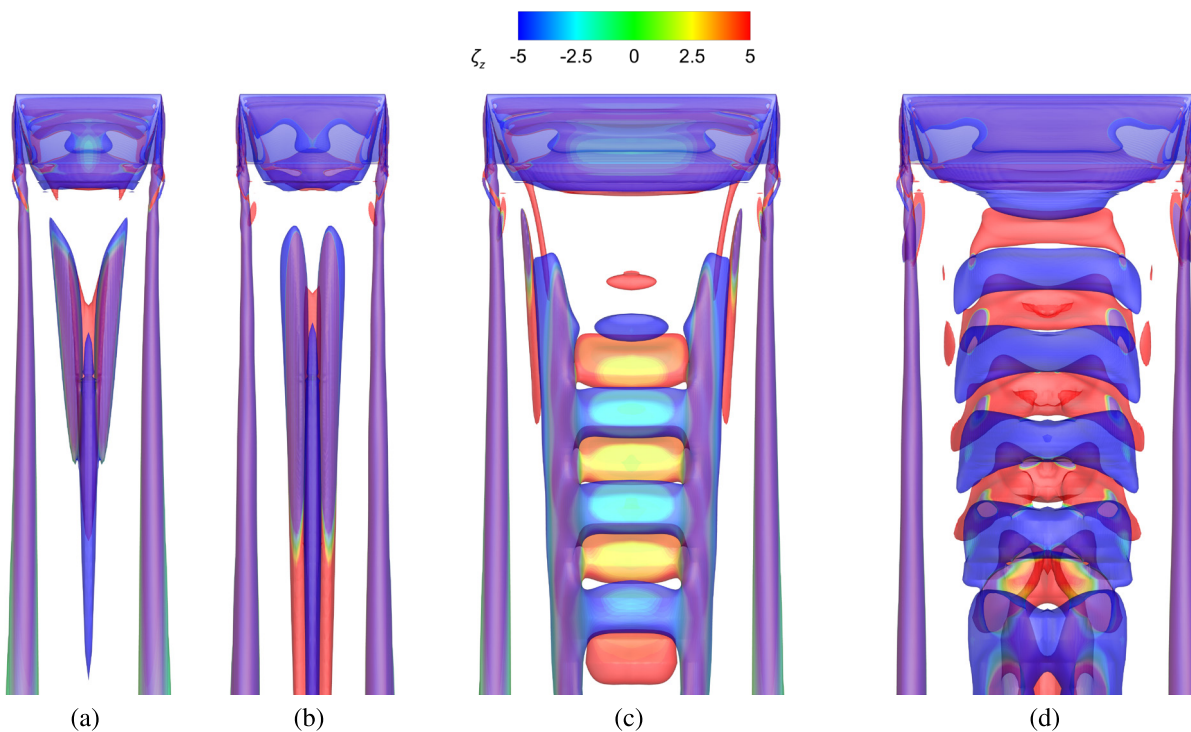


FIGURE 14. Top view of the vortical structure for (a) $sAR = 1, Re = 1 \times 10^4$, (b) $sAR = 1, Re = 4 \times 10^4$, (c) $sAR = 2, Re = 1 \times 10^4$, and (d) $sAR = 2, Re = 4 \times 10^4$ at $\alpha = 15^\circ$. The isosurface of $Q = 0.25$ is visualised and colored with $\zeta_z = \pm 5$. The full span wings are displayed for better visualization by applying a mirror on the root.

phase, primarily due to vortex shedding. The unsteadiness in the flowfield is mostly quantified by Strouhal number

(St) [59], [60]. The Strouhal number is the nondimensional vortex shedding frequency of the separated flow past a bluff

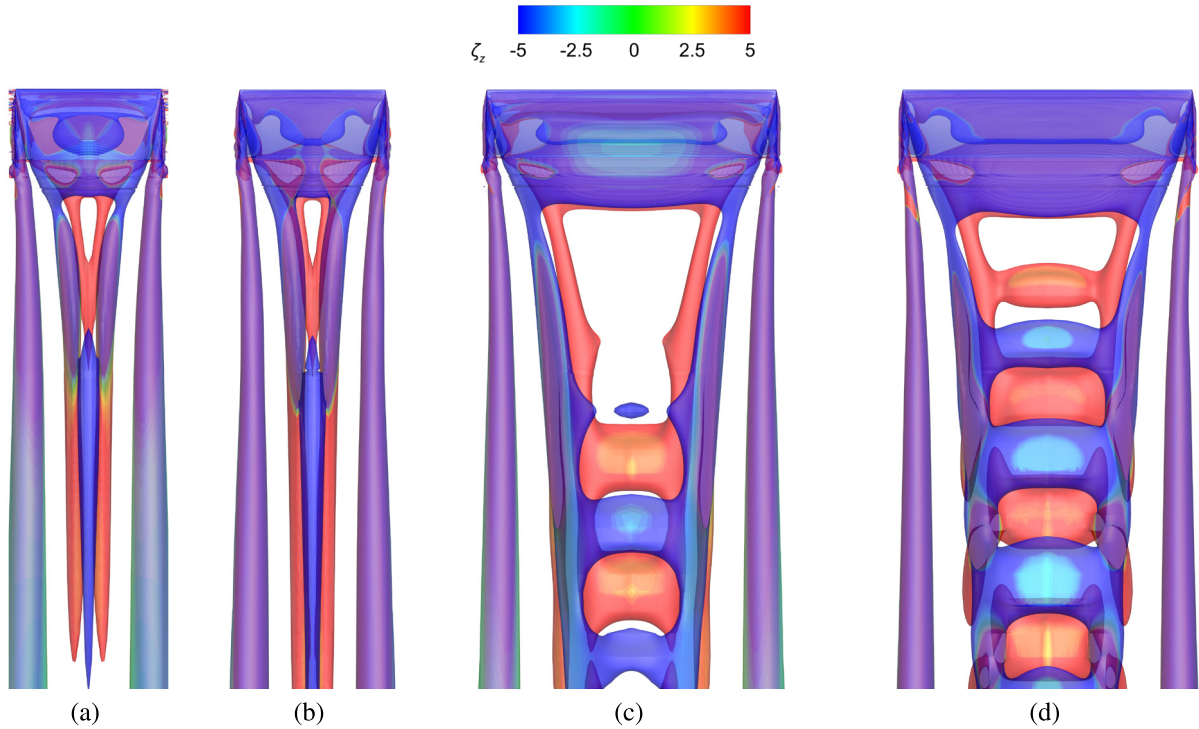


FIGURE 15. Top view of the vortical structure for (a) $sAR = 1, Re = 1 \times 10^4$, (b) $sAR = 1, Re = 4 \times 10^4$, (c) $sAR = 2, Re = 1 \times 10^4$, and (d) $sAR = 2, Re = 4 \times 10^4$ at $\alpha = 20^\circ$. The isosurface of $Q = 0.25$ is visualised and colored with $\zeta_z = \pm 5$. The full span wings are displayed for better visualization by applying a mirror on the root.

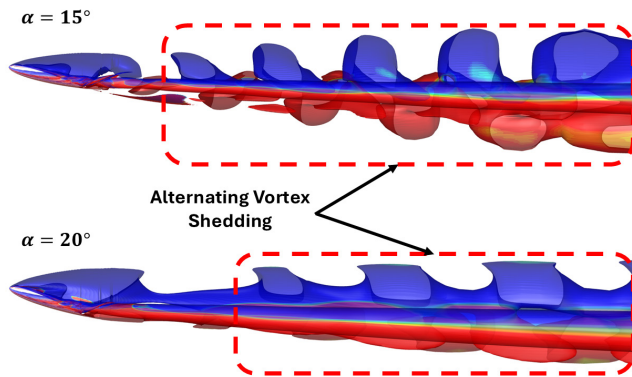


FIGURE 16. Side view of the vortical structure for (a) $sAR = 2, Re = 4 \times 10^4$ at $\alpha = 15^\circ$ and 20° .

body and is defined as $St = f_v c / U_\infty$. In this definition, f_v denotes the vortex shedding frequency, which is determined from the amplitude spectrum of C_L and corresponds to the peak amplitude in the spectrum. Figure 11 shows the relation between Strouhal number and angle of attack for 2D airfoil case and the finite wing with $sAR = 2$ at $Re = 1 \times 10^4$ and 4×10^4 .

Figure 12 presents the separated flow regions on several spanwise contours and specific dissipation rate (ω) contours on the various slices at the wake of the wing at $Re = 4 \times 10^4$ and $\alpha = 20^\circ$. The regions of low specific dissipation

rate indicate that the dissipation of turbulent kinetic energy is weak locally and that separated shear layers are more susceptible to instability. However, in the present cases, this does not directly cause but is related to the unsteadiness. For $sAR = 1$, the strong downwash from the tip vortex stabilizes the separated shear layer, and the wake remains steady. On the other hand, for $sAR = 2$, the weak dissipation region significantly contains larger region than $sAR = 1$ wing and expands towards the root due to weaker downwash. The vortical structures around and the wake of the finite wings are identified by using an isosurface of $Q (= 0.25)$ criterion colored with spanwise vorticity ($\zeta_z = \pm 5$) contours and shown in Figures 13-15. The full span wings are displayed for better visualization by applying a mirror on the symmetry plane at the root. For $sAR = 1$, the flow remains steady regardless of Reynolds number and angle of attack in our analyzed range. Such steady flows generate a pair of tip vortices that produce significant downwash across the wing span, thereby inhibiting the development of prominent leading-edge vortices. Therefore, the strong central cell without vortex shedding occurs. Taira and Colonius [12] found that the flat plate wing with $AR = 2$ exhibits steady wakes for $\alpha < 20^\circ$ and $\alpha < 15^\circ$ at $Re = 3 \times 10^2$ and 5×10^2 , respectively. Zhang et al. [13], [61] and Zhang and Taira [51] also observed that the flow remains stable up to $\alpha = 18^\circ$, with a steady tip vortex and vortex shedding near the midspan at that angle for a NACA0015 wing with $sAR = 1$ at $Re = 4 \times 10^2$. The unsteadiness begins at

$\alpha = 10^\circ$ and $Re = 1 \times 10^3$ for a NACA0012 wing with $sAR = 1$ according to Pandi and Mittal's [15] high-order numerical simulations. The discrepancy in the unsteadiness at higher Reynolds numbers is attributed to the small-scale eddy structures that cannot be captured by URANS simulations.

For $sAR = 2$, as the aspect ratio increases, the tip vortex induces weaker downwash near the midspan, and the unsteady flow is observed under all conditions except at $\alpha = 10^\circ$ and $Re = 1 \times 10^4$. It can be said that the critical angle of attack (α_{cr}), where the vortex shedding is initially observed [59], [62], coincides in the interval of $10^\circ < \alpha_{cr} \leq 14^\circ$ at $Re = 1 \times 10^4$. On the other hand, $sAR = 2$ wing exhibits $\alpha_{cr} \geq 10^\circ$ at $Re = 4 \times 10^4$. This illustrates the decreasing trend of α_{cr} with increasing Reynolds number. Periodic oscillations with very small amplitude are observed in the time histories of the aerodynamic coefficients. The reason is that the alternating Karman vortex street (successive counter-rotating vortices, clockwise vortices at the top and counterclockwise vortices at the bottom) forms downstream; thus, its influence on the surface forces remains limited. Figure 16 also highlights the regions where these vortices develop. The Strouhal number decreases with increasing angle of attack (Figure 11), indicating a reduction in vortex shedding frequency. This trend is clearly seen in the Q -criterion isosurfaces (see Figures 13d-15d).

IV. CONCLUSION

This study numerically investigated the transitional, three-dimensional separated flow over NACA0012 wings with low aspect ratios ($sAR = 1$ and 2) at low Reynolds numbers of $Re = 1 \times 10^4$ and 4×10^4 , across a range of angles of attack. The simulations revealed a complex interplay between tip vortex-induced downwash, aspect ratio, and Reynolds number in shaping aerodynamic performance, laminar separation bubble dynamics, and wake behavior.

The lower aspect ratio wing ($sAR = 1$) consistently produced smaller lift and drag coefficients than $sAR = 2$, independent of Reynolds number. For $sAR = 1$, the lift coefficient increased monotonically with angle of attack, while $sAR = 2$ displayed a non-monotonic trend due to the early onset of unsteady flow. A rootward shift of the sectional lift coefficient peak was observed in the $sAR = 1$ wing, indicating a broader influence of tip vortices on the spanwise flow field.

LSB analysis showed that as aspect ratio increased, the separation and transition points moved upstream, and the bubble length decreased. The stronger downwash in the $sAR = 1$ configuration delayed both separation and transition near the root but suppressed vortex shedding across the span, resulting in steady wakes under all test conditions. Conversely, the $sAR = 2$ wing experienced unsteady flow and Kármán vortex shedding, particularly at higher angles of attack and Reynolds numbers.

Overall, this work highlights the stabilizing effect of strong tip vortex-induced downwash in low-aspect-ratio wings and its influence on delaying separation, suppressing

wake unsteadiness, and shaping spanwise aerodynamic distributions. These insights contribute to a better understanding of low-Reynolds-number aerodynamics relevant to micro air vehicle design and other low-speed flight applications.

ACKNOWLEDGMENT

The authors would like to thank the King Abdullah University of Science and Technology (KAUST), Supercomputing Laboratory, and HPC Resources, for providing computing resources.

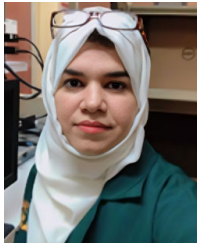
REFERENCES

- [1] W. Shyy, Y. Lian, J. Tang, D. Viieru, and H. Liu, *Aerodynamics Low Reynolds Number Flyers*. Cambridge, U.K.: Cambridge Univ. Press, 2007.
- [2] J. Grasmeyer and M. Keennon, "Development of the black widow micro air vehicle," in *Proc. 39th Aerosp. Sci. Meeting Exhib.*, 2001, p. 127.
- [3] H. Wu, D. Sun, and Z. Zhou, "Micro air vehicle: Configuration, analysis, fabrication, and test," *IEEE/ASME Trans. Mechatronics*, vol. 9, no. 1, pp. 108–117, Mar. 2004.
- [4] K. D. Jones, C. J. Bradshaw, J. Papadopoulos, and M. F. Platzer, "Bio-inspired design of flapping-wing micro air vehicles," *Aeronaut. J.*, vol. 109, no. 1098, pp. 385–393, Aug. 2005.
- [5] K. Sibilski, M. Nowakowski, D. Rykaczewski, P. Szczepaniak, A. Zyluk, A. Sibilska-Mroziewicz, M. Garbowski, and W. Wróblewski, "Identification of fixed-wing micro aerial vehicle aerodynamic derivatives from dynamic water tunnel tests," *Aerospace*, vol. 7, no. 8, p. 116, Aug. 2020.
- [6] A. N. de Lucena, B. M. F. da Silva, and L. M. G. Gonçalves, "Micro aerial vehicle with basic risk of operation," *Sci. Rep.*, vol. 12, no. 1, p. 12772, Jul. 2022.
- [7] G. E. Torres and T. J. Mueller, "Low-aspect-ratio wing aerodynamics at low Reynolds numbers," *AIAA J.*, vol. 43, no. 5, pp. 865–873, 2004.
- [8] M. Mizoguchi and H. Itoh, "Effect of aspect ratio on aerodynamic characteristics at low Reynolds numbers," *AIAA J.*, vol. 51, no. 7, pp. 187–1639, Jul. 2013.
- [9] G. K. Ananda, P. P. Sukumar, and M. S. Selig, "Measured aerodynamic characteristics of wings at low Reynolds numbers," *Aerosp. Sci. Technol.*, vol. 42, pp. 392–406, Apr. 2015.
- [10] M. Okamoto and A. Azuma, "Aerodynamic characteristics at low Reynolds numbers for wings of various planforms," *AIAA J.*, vol. 51, no. 7, pp. 1631–1639, 2011.
- [11] M. Mizoguchi, D. Sasaki, M. Kamikubo, and R. Fujii, "Effect of Aspect Ratio on Aerodynamic Characteristics at Low Reynolds Numbers," *Trans. Jpn. Soc. Aeronaut. Space Sci.*, vol. 62, no. 6, pp. 310–317, 2019.
- [12] K. Taira and T. Colonius, "Three-dimensional flows around low-aspect-ratio flat-plate wings at low Reynolds numbers," *J. Fluid Mech.*, vol. 623, pp. 187–207, Mar. 2009.
- [13] K. Zhang, S. Hayostek, M. Amitay, W. He, V. Theofilis, and K. Taira, "On the formation of three-dimensional separated flows over wings under tip effects," *J. Fluid Mech.*, vol. 895, p. 9, Jul. 2020.
- [14] L. Smith and K. Taira, "The effect of Reynolds number on the separated flow over a low-aspect-ratio wing," *J. Fluid Mech.*, vol. 992, p. 2, Aug. 2024.
- [15] J. S. S. Pandi and S. Mittal, "Streamwise vortices, cellular shedding and force coefficients on finite wing at low Reynolds number," *J. Fluid Mech.*, vol. 958, p. 10, Mar. 2023.
- [16] Y. Zhu, J. Wang, and J. Liu, "Tip effects on three-dimensional flow structures over low-aspect-ratio plates: Mechanisms of spanwise fluid transport," *J. Fluid Mech.*, vol. 983, p. 35, Mar. 2024.
- [17] Y. Zhu, J. Wang, Y. Xu, Y. Qu, and Y. Long, "Swallow-tailed separation bubble on a low-aspect-ratio trapezoidal plate: Effects of near-wall spanwise flow," *J. Fluid Mech.*, vol. 965, p. 12, Jun. 2023.
- [18] A. M. Edstrand, Y. Sun, P. J. Schmid, K. Taira, and L. N. Cattafesta, "Active attenuation of a trailing vortex inspired by a parabolized stability analysis," *J. Fluid Mech.*, vol. 855, p. 2, Nov. 2018.
- [19] A. Burtsev, V. Pezlar, and V. Theofilis, "Sensitivity of flows over three-dimensional swept wings at low Reynolds number," *J. Fluid Mech.*, vol. 997, p. 11, Oct. 2024.
- [20] J. H. M. Ribeiro, C.-A. Yeh, and K. Taira, "Triglobal resolvent analysis of swept-wing wakes," *J. Fluid Mech.*, vol. 954, p. 42, Jan. 2023.

- [21] J. H. M. Ribeiro and K. Taira, "Triglobal resolvent-analysis-based control of separated flows around low-aspect-ratio wings," *J. Fluid Mech.*, vol. 995, p. 13, Sep. 2024.
- [22] I. Tani, "Low-speed flows involving bubble separations," *Prog. Aerosp. Sci.*, vol. 5, pp. 70–103, Jan. 1964.
- [23] H. P. Horton, "Laminar separation bubbles in two and three dimensional incompressible flow," Ph.D. dissertation, Dept. Aeronaut. Eng., University of London, London, U.K., 1968.
- [24] M. Gaster, "The structure and behaviour of laminar separation bubbles," Aeronautical Res. Council (A.R.C.), London, U.K., Tech. Rep. 3595, 1967.
- [25] S. C. Yen and L. C. Huang, "Flow patterns and aerodynamic performance of unswept and swept-back wings," *J. Fluids Eng.*, vol. 131, no. 11, 2009, Art. no. 111101.
- [26] M. Awasthi, D. J. Moreau, and C. J. Doolan, "Flow structure of a low aspect ratio wall-mounted airfoil operating in a low Reynolds number flow," *Experim. Thermal Fluid Sci.*, vol. 99, pp. 94–116, Dec. 2018.
- [27] J. W. Kurelek, M. Kotsonis, and S. Yarusevych, "Transition in a separation bubble under tonal and broadband acoustic excitation," *J. Fluid Mech.*, vol. 853, pp. 1–36, Oct. 2018.
- [28] T. Michelis, S. Yarusevych, and M. Kotsonis, "On the origin of spanwise vortex deformations in laminar separation bubbles," *J. Fluid Mech.*, vol. 841, pp. 81–108, Apr. 2018.
- [29] C. E. Toppings and S. Yarusevych, "Structure and dynamics of a laminar separation bubble near a wingtip," *J. Fluid Mech.*, vol. 929, p. 36, Dec. 2021.
- [30] C. E. Toppings, J. W. Kurelek, and S. Yarusevych, "Laminar separation bubble development on a finite wing," *AIAA J.*, vol. 59, no. 8, pp. 2855–2867, Aug. 2021.
- [31] C. E. Toppings and S. Yarusevych, "Structure and dynamics of a laminar separation bubble near a wing root: Towards reconstructing the complete LSB topology on a finite wing," *J. Fluid Mech.*, vol. 944, p. 14, Aug. 2022.
- [32] A. Grille Guerra, C. Mertens, J. Little, and B. van Oudheusden, "Experimental characterization of an unsteady laminar separation bubble on a pitching wing," *Experim. Fluids*, vol. 64, no. 1, p. 16, Jan. 2023.
- [33] C. E. Toppings and S. Yarusevych, "Laminar separation bubble formation and bursting on a finite wing," *J. Fluid Mech.*, vol. 986, p. 26, May 2024.
- [34] A. M. and N. D. Sandham, "Laminar separation bubble development on a finite wing," *J. Fluid Mech.*, vol. 410, pp. 1–28, Aug. 2000.
- [35] J. N. N. Counsil and K. Goni Boulama, "Low-Reynolds-number aerodynamic performances of the NACA 0012 and Selig–Donovan 7003 airfoils," *J. Aircr.*, vol. 50, no. 1, pp. 204–216, Jan. 2013.
- [36] J. AlMutairi, E. ElJack, and I. AlQadi, "Dynamics of laminar separation bubble over NACA-0012 airfoil near stall conditions," *Aerosp. Sci. Technol.*, vol. 68, pp. 193–203, Sep. 2017.
- [37] D. Rodríguez and E. M. Gennaro, "Enhancement of disturbance wave amplification due to the intrinsic three-dimensionalisation of laminar separation bubbles," *Aeronaut. J.*, vol. 123, no. 1268, pp. 1492–1507, Oct. 2019.
- [38] E. Eljack, J. Soria, Y. Elawad, and T. Ohtake, "Simulation and characterization of the laminar separation bubble over a NACA-0012 airfoil as a function of angle of attack," *Phys. Rev. Fluids*, vol. 6, no. 3, Mar. 2021, Art. no. 034701.
- [39] B. Anilir and D. F. Kurtulus, "Unsteady aerodynamic performance of SD7062 airfoil at high Reynolds number," *Prog. Comput. Fluid Dyn., Int. J.*, vol. 23, no. 2, pp. 65–86, 2023.
- [40] E. M. Eljack, "The structure and dynamics of the laminar separation bubble," *J. Fluid Mech.*, vol. 998, p. 56, Nov. 2024.
- [41] J. S. S. Pandi and S. Mittal, "Twisted finite wing at low Reynolds number: Cellular vortex shedding, wing-tip vortex and aerodynamic performance," *J. Fluid Mech.*, vol. 1002, p. 28, Jan. 2025.
- [42] *ANSYS Fluent User's Guide, 23.2*, Ansys Inc., Canonsburg, PA, USA, 2023.
- [43] A. Kilavuz, M. Ozgoren, L. A. Kavurmacioglu, T. Durhasan, F. Sarigiguzel, B. Sahin, H. Akilli, E. Sekeroglu, and B. Yaniktepe, "Flow characteristics comparison of PIV and numerical prediction results for an unmanned underwater vehicle positioned close to the free surface," *Appl. Ocean Res.*, vol. 129, Dec. 2022, Art. no. 103399.
- [44] J. H. Ferziger, M. Peric, and R. L. Street, *Computational Methods for Fluid Dynamics*. Cham, Switzerland: Springer, 2020.
- [45] F. R. Menter, "Two-equation eddy-viscosity turbulence models for engineering applications," *AIAA J.*, vol. 32, no. 8, pp. 1598–1605, Aug. 1994.
- [46] R. B. Langtry and F. R. Menter, "Correlation-based transition modeling for unstructured parallelized computational fluid dynamics codes," *AIAA J.*, vol. 47, no. 12, pp. 2894–2906, Dec. 2009.
- [47] K. Zore, A. Matyushenko, S. Shah, C. Aliaga, J. Stokes, and F. Menter, "Laminar–Turbulent transition prediction on industrial computational fluid dynamics applications," *J. Aircr.*, vol. 60, no. 1, pp. 1–20, Jan. 2023.
- [48] B. Anilir, D. F. Kurtulus, and M. F. Platzer, "Flow control by oscillating trailing-edge flaps," *AIAA J.*, vol. 61, no. 9, pp. 4210–4213, Sep. 2023.
- [49] B. Anilir, D. F. Kurtulus, and M. F. Platzer, "The oscillating vortex generator: A boundary layer propulsion and flow control device," *Aeronaut. J.*, vol. 129, no. 1332, pp. 380–394, Feb. 2025.
- [50] M. Güney, B. Anilir, and D. F. Kurtulus, "Computational investigation of low-Reynolds-number unsteady flows past NACA 0012," *Prog. Comput. Fluid Dyn., Int. J.*, vol. 26, no. 1, pp. 32–47, 2026.
- [51] K. Zhang and K. Taira, "Laminar vortex dynamics around forward-swept wings," *Phys. Rev. Fluids*, vol. 7, no. 2, Feb. 2022, Art. no. 024704.
- [52] H. B. Helmbold, "Der unverwundene ellipsenflugel als tragende flanche," *Jahrbuch 1942 der Deutch Luftfahrtforsch.*, pp. II11–II13, 1942.
- [53] J.-J. Lee, C.-T. Hsieh, C. C. Chang, and C.-C. Chu, "Vorticity forces on an impulsively started finite plate," *J. Fluid Mech.*, vol. 694, pp. 464–492, Mar. 2012.
- [54] M. S. H. Boutilier and S. Yarusevych, "Measured aerodynamic characteristics of wings at low Reynolds number: Parametric study of separation and transition characteristics over an airfoil at low Reynolds numbers," *Experim. Fluids*, vol. 52, pp. 1491–1506, Jan. 2012.
- [55] M. M. O'Meara and T. J. Mueller, "Laminar separation bubble characteristics on an airfoil at low Reynolds numbers," *AIAA J.*, vol. 25, no. 8, pp. 1033–1041, Aug. 1987.
- [56] B. McAuliffe and M. I. Yaras, "Separation-bubble-transition measurements on a low-re airfoil using particle image velocimetry," *Turbo Expo*, vol. 3, pp. 1029–1038, Jun. 2005.
- [57] M. Ol, B. McCauliffe, E. Hanff, U. Scholz, and C. Kaehler, "Comparison of laminar separation bubble measurements on a low Reynolds number airfoil in three facilities," in *Proc. 35th AIAA Fluid Dyn. Conf. Exhib.*, Jun. 2005, p. 5149.
- [58] R. Hain, C. J. Kähler, and R. Radespiel, "Dynamics of laminar separation bubbles at low-Reynolds-number aerofoils," *J. Fluid Mech.*, vol. 630, pp. 129–153, Jul. 2009.
- [59] D. F. Kurtulus, "On the unsteady behavior of the flow around NACA 0012 airfoil with steady external conditions at $Re=1000$," *Int. J. Micro Air Vehicles*, vol. 7, no. 3, pp. 301–326, Sep. 2015.
- [60] A. Roshko, "On the wake and drag of bluff bodies," *J. Aeronaut. Sci.*, vol. 22, no. 2, pp. 124–132, Feb. 1955.
- [61] K. Zhang, S. Hayostek, M. Amitay, A. Burtsev, V. Theofilis, and K. Taira, "Laminar separated flows over finite-aspect-ratio swept wings," *J. Fluid Mech.*, vol. 905, p. 1, Dec. 2020.
- [62] T. Kouser, D. F. Kurtulus, A. Aliyu, S. Goli, L. M. Alhems, I. H. Imran, and A. M. Memon, "Unsteady aerodynamics over NACA0005 airfoil for ultra-low Reynolds numbers," *IEEE Access*, vol. 12, pp. 83658–83674, 2024.



BERKAN ANILIR received the B.Sc. and M.Sc. degrees from the Aerospace Engineering Department, Middle East Technical University (METU), in 2021 and 2023, respectively, where he is currently pursuing the Ph.D. degree. He is also a Graduate Research Assistant with the Aerospace Engineering Department. His research interests include unsteady aerodynamics, computational fluid dynamics, and aircraft design.



tion, unsteady aerodynamics, and aeroacoustics.

TAIBA KOUSER was born in Faisalabad, Pakistan. She received the Ph.D. degree from the School of Aerospace Engineering, Huazhong University of Science and Technology, Wuhan, China, in 2021. Currently, she is a Postdoctoral Researcher with the Applied Research Center for Metrology, Standards and Testing (ARC-MST), King Fahd University of Petroleum and Minerals (KFUPM), Dhahran, Saudi Arabia. Her research interests include computational fluid dynamics, drag reduction, unsteady aerodynamics, and aeroacoustics.



Since 2018, she has been a Professor with the Department of Aerospace Engineering, Middle East Technical University. Her research interests include aircraft design, unsteady aerodynamics, and uncrewed air vehicles. She was a recipient of the Amelia Earhart Fellow at Zonta International, in 2005, the NATO Scientific Achievement Award, in 2011, the Turkish Academy of Science Young Scientific Award, in 2012, and the Zonta International Centennial Recognition Award of Turkey, in 2019.

DILEK FUNDA KURTULUS received the B.S. and M.S. degrees in aerospace engineering from Middle East Technical University, Ankara, Türkiye, in 2000 and 2002, respectively, and the Ph.D. degree in aerospace engineering from the ENSMA/Université de Poitiers, Poitiers, France. In 2006, she was Postdoctoral Researcher with the Laboratoire d'Études Aérodynamique, ENSMA Poitiers, and Laboratoire de Combustion et Systèmes Réactifs, CNRS, Orléans, France.



He is currently a Postdoctoral Researcher with the Applied Research Center for Metrology, Standards and Testing (ARC-MST), King Fahd University of Petroleum and Minerals (KFUPM), Saudi Arabia. His research interests include aircraft design, experimental and numerical fluid dynamics, and uncrewed air vehicles. He has memberships in professional societies, such as the National Society of Fluid Mechanics and Fluid Power, the Indian Society of Theoretical and Applied Mechanics, and the Aeronautical Society of India.

SRIKANTH GOLI was born in Hyderabad, India. He received the B.Tech. degree in aeronautical engineering from Jawaharlal Nehru Technological University, in 2008, the M.E. degree in aeronautical engineering from the Hindustan Institute of Technology and Science, in 2011, and the Ph.D. degree from the Department of Aerospace Engineering, IIT Kharagpur, India, in 2019. From 2019 to 2022, he carried out research at various academic institutions and industries. He is



He is currently a Research Engineer III with KFUPM and affiliated with the Department of Control and Instrumentation Engineering, where he teaches intelligent process control and industrial Internet of Things for M.S. programs. He holds two U.S. patents and has several peer-reviewed publications. His research interests include guided-wave EMAT NDT, physics-informed signal processing, intelligent process control, AI/ML for monitoring, digital twins, GIS-based water analytics, and IoT sensing and control systems.

MUHAMMAD SABIH received the B.E. degree in industrial electronics from IIEE-NED University, Pakistan, in 2000, and the M.S. and Ph.D. degrees in systems engineering from the King Fahd University of Petroleum and Minerals (KFUPM), Dhahran, Saudi Arabia, in 2009 and 2014, respectively. He worked with the ROSEN Group as a Sensor and Algorithm Specialist, developing Python-based signal processing and machine learning algorithms for pipeline inspection.



He is currently an Assistant Professor with the Department of Electrical Engineering, King Fahd University, Saudi Arabia. His research interests include networked control systems, multi-agent systems, nonlinear control, and adaptive control.

IMIL HAMDA IMRAN received the B.S. degree in electrical engineering from Andalas University, Indonesia, in 2011, the M.S. degree in systems and control engineering from the King Fahd University of Petroleum and Minerals, Saudi Arabia, in 2015, and the Ph.D. degree in electrical engineering from The University of Newcastle, Australia, in 2020. He was a Postdoctoral Researcher with Lancaster University, U.K., and King Fahd University of Petroleum and Minerals, from 2020 to 2024.



From 2009 to 2010, he was a Research Engineer with NUS and a Lecturer, in 2011. He joined the Research and Development Department, Rosen Group, as a Sensors and Algorithm Specialist. In 2019, he joined KFUPM as an Assistant Professor, where he is actively participating in managing various client-funded and internally funded research projects and teaching. He has authored or co-authored several peer-reviewed research articles and conference papers in reputable journals and international conferences. His research interests include control systems, signal processing, data analytics, nondestructive testing, and aquaponics. For more information visit the link (www.azharmemon.com).

AZHAR M. MEMON was born in Pakistan, in 1987. He received the B.E. degree in electronics from the National University of Sciences and Technology (NUST), Pakistan, in 2009, the M.Sc. degree in automation and control engineering from the National University of Singapore (NUS), Singapore, in 2010, and the Ph.D. degree from the King Fahd University of Petroleum and Minerals (KFUPM), Saudi Arabia, in 2015.



He has authored or co-authored more than 180 journal articles and patents. His research interests include gas turbines, energy systems, failure analysis, wind energy, and energy conservation.

LUAI M. ALHEMS received the Ph.D. degree from Texas A&M University, College Station, TX, USA, in 2002. He is currently a Professor in thermo-fluid with the Department of Mechanical Engineering, King Fahd University of Petroleum and Minerals (KFUPM), Dhahran, Saudi Arabia. He is also the Director of the Applied Research Center for Metrology, Standards and Testing (ARC-MST) Research Institute. Regional authorities have recognized him for his research work.